Optics Letters

Single-step etched two-dimensional polarization splitting dual-band grating coupler for wavelength (de)multiplexing

Guanglian Cheng,[1] Qiyuan Yi,[1] Qiyuan Li,[1] Zhiwei Yan,[1] Fanglu Xu,[1] Yongchao Zou,[2] Ting Li,[3] Yi Zou,[3,4] Yu Yu,[1] and Li Shen[1,*]

[1]Wuhan National Laboratory for Optoelectronics and School of Optical and Electronic Information, Huazhong University of Science and Technology, Wuhan, Hubei 430074, China
[2]College of Meteorology and Oceanography, National University of Defense Technology, Changsha, Hunan 410073, China
[3]School of Information Science and Technology, ShanghaiTech University, Shanghai 201210, China
[4]e-mail: zouyi@shanghaitech.edu.cn
*Corresponding author: lishen@hust.edu.cn

Received 3 May 2022; revised 10 July 2022; accepted 10 July 2022; posted 11 July 2022; published 28 July 2022

Diffractive periodic-structure-based grating couplers (GCs) are the most widely used devices for light coupling between optical fibers and integrated photonic devices. However, conventional GCs have limited wavelength operation and are polarization specific, which is due to the intrinsic radiation angle dependency on both wavelength and polarization. Here we propose and experimentally demonstrate a polarization-splitting dual-band grating coupler (PS-DBGC) for polarization diversity and wavelength division (de)multiplexing (WDM) operation. The four-port two-dimensional PS-DBGC is based on a periodically arranged structure with square holes, and requires only a single etch step in a 340-nm silicon-on-insulator platform. The simulation predicts that the maximum coupling efficiency (CE) of the proposed PS-DBGC is −2.8 dB and −4.6 dB for the O- and C-band, respectively. The measured peak CEs of the fabricated device are −4.7 dB at 1280 nm and −8.4 dB at 1522 nm. We anticipate that this PS-DBGC could potentially improve the performance of any future integrated WDM passive optical network.

https://doi.org/10.1364/OL.462937

In light of the employment of the wavelength division multiplexing (WDM) technique for large-capacity optical communications [1], optical components which are capable of operating over broadband bandwidth or multiple spectral bands are highly desirable. For an example, two or more wavelengths near the 1310-, 1490-, or 1550-nm bands are typically used in WDM passive optical network (PON) systems, thus requiring optical components that can efficiently operate in at least two of these wave bands with 100- to 300-nm wavelength separation [2]. Currently, WDM PON systems are based on bulk optics and the expensive components required hinder its practical application [3]. Multiplexing on a silicon photonic chip and directly interfacing with optical fibers can simplify packaging and greatly reduce the cost for O-band (1260–1360 nm) and C-band (1530–1565 nm) transceivers used in PON systems [4]. Silicon-on-insulator (SOI) grating couplers (GCs) are key components for efficient fiber-to-chip interconnection [5,6]. However, due to diffractive structures, GCs usually suffer from limited operation bandwidth up to an order of a few tens of nanometers [7,8] and high polarization sensitivity. Hence, there remains a tough challenge for simultaneously coupling light with arbitrary polarization at two widely separated wavelengths into integrated devices and vice versa.

To address the two issues, GCs capable of multi-wavelength band transmission and polarization-diversity operation were initially proposed by Roelkens *et al.* [9], and have attracted growing attention in the past few years [10]. There have been reports of various dual-band GCs for on-chip wavelength (de)multiplexers, including coupling and demultiplexing into opposite [9,11] or orthogonal directions [12,13]. More recently, subwavelength (SWG) structure based GCs have been demonstrated which can couple two wavelength bands into a same waveguide [14,15]. To tackle the polarization sensitivity, 1D GCs with polysilicon overlay [10] or backside metal mirrors [16] have been proposed. In addition, two-dimensional GCs can couple orthogonal polarization light into the same waveguide mode [17–20]. So far, there are very few polarization-splitting GCs that can operate in dual-wavelength-band mode except a bi-wavelength polarization-splitting GC making use of the TE mode for 1550 nm and TM mode for 1310 nm [21]. An SWG dual-band GC with two different etch depths has been theoretically proposed as a polarization-independent wavelength splitter [22]. Nevertheless, the TM mode was introduced in both schemes, which requires additional handing such as polarization-rotating operation after coupling.

In this Letter, we propose and demonstrate bi-wavelength polarization splitting based on a compact two-dimensional GC patterned with periodically arranged square holes. The four-port polarization-splitting dual-band grating coupler (PS-DBGC) can simultaneously couple the O- and C-band light into the corresponding waveguide port in the TE mode with the same incident angle. For X-/Y-/S-/P-polarizations, simulations show that the device exhibits maximum coupling efficiency (CE)

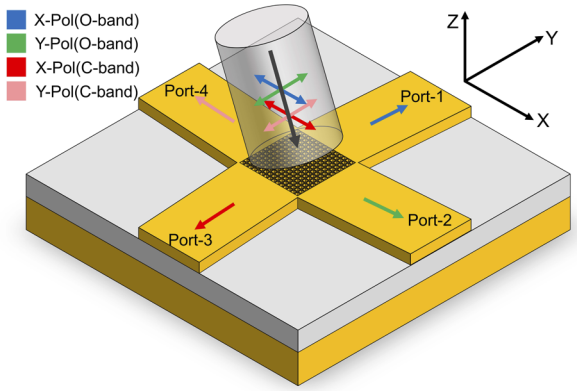

Fig. 1. 3D schematic view of the PS-DBGC.

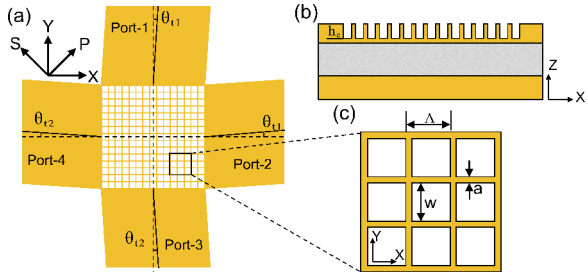

Fig. 2. (a) Top view of the PS-DBGC. (b) Cross sectional view shown as marked by the horizontal or vertical dashed lines in panel (a). (c) Partial zoom-out view of the PS-DBGC.

of −2.8 dB and −4.6 dB for the O- and C-band. The footprint of the device is $\sim 10 \times 10\ \mu m^2$. Experimentally, −4.7-dB and −8.4-dB peak CEs are demonstrated at 1280 nm and 1522 nm, respectively. The proposed PS-DBGC can pave the way toward low-cost WDM PON systems using monolithically silicon integrated optical components.

The proposed PS-DBGC is designed based on an SOI wafer with a 340-nm-thick top silicon layer and a 2-μm-thick buried oxide layer, as well as a 1-μm-thick silica upper cladding. The 340-nm-thick SOI wafer is used here because it is possible to meet the phase-matching conditions required for dual-band and dual-polarization operation. The operation schematic of the PS-DBGC is illustrated in Fig. 1. It consists of a two-dimensional square grating section and four output ports. Port-1 and port-2 function like a polarization-splitting grating coupler (PSGC) for the O-band, where X-polarization and Y-polarization are output from port-1 and port-2, respectively. In contrast, port-3 and port-4 function like a PSGC for the C-band, where X-polarization and Y-polarization are output from port-3 and port-4, respectively. S-polarization or P-polarization can be regarded as the superposition of X-polarization and Y-polarization, and they are equally distributed into port-1 and port-2 for the O-band or port-3 and port-4 for the C-band. S- and P-polarizations are considered here to illustrate that the proposed PS-DBGC possesses the polarization-independent function, thus realizing polarization diversity for the dual-band operation [23]. Moreover, light with arbitrary polarization can also be coupled into separate waveguides with different splitting ratios. The light is coupled into the corresponding ports with a fixed TE polarization, connected to a single mode rib waveguide via linear adiabatic tapers with a length of $L_{taper} = 300\ \mu m$ to minimize the transition loss.

Figure 2(a) shows the top view of the PS-DBGC, which is a two-dimensional array of periodically arranged square holes with period Λ and width w. The incident angle of the single-mode fiber (SMF) is chosen as $\theta = 17°$ and the SMF is placed in the plane that bisects the array at 45° to create a symmetric condition. Due to the fiber tilt angle, a deviation from the x axis and y axis is observed in the propagation direction of the coupled light for different ports. Therefore, we slightly tilt the two waveguides that connect port-1 and port-2 away by $\theta_{t1} = 4°$, and the waveguides that connect port-3 and port-4 by $\theta_{t2} = 4.5°$ to align with the propagation directions, as also depicted in Fig. 2(a). The cross sectional view shown by the dashed line and the partially enlarged view of the PS-DBGC are also illustrated in Figs. 2(b) and 2(c). Here, the etch depth of the whole device is set to be $h_e = 270$ nm.

The origin of the dual-wavelength-band polarization diversity operation can be derived from the phase-matching conditions for grating diffraction. For two wavelengths λ_1 and λ_2, the phase-matching conditions can be written as

$$n_{eff1} - sin\theta = \frac{\lambda_1}{\Lambda}, \tag{1}$$

$$n_{eff2} - sin(-\theta) = \frac{\lambda_2}{\Lambda}, \tag{2}$$

where n_{eff1} and n_{eff2} are the effective refractive indices of fundamental Floquet–Bloch modes supported by the periodic structure. By combining these phase-matching conditions in Eqs. (1) and (2) and eliminating the grating pitch Λ, the relationship of the two allowed wavelengths can be expressed as

$$\frac{n_{eff1} - sin\theta}{n_{eff2} + sin\theta} = \frac{\lambda_1}{\lambda_2}. \tag{3}$$

By adjusting the grating period Λ and duty cycle $DC = a/\Lambda$, n_{eff1} and n_{eff2} can be appropriately tailored to satisfy Eq. (3).

To obtain appropriate structure parameters for dual-band operation in the O- and C-band, the three-dimensional finite-difference time-domain (3D-FDTD) method is used for calculation. Owing to the symmetry of PS-DBGC, one can choose either X-polarization or Y-polarization as the input polarization for optimization, which will return the same results. The optimal Λ and DC can be obtained through sweeping the whole parameter space and evaluating the performance for each parameter set using electromagnetic simulation. Figure 3(a) shows the calculated peak CE as a function of Λ and DC in the wavelength range of 1290–1330 nm. Similarly, Fig. 3(b) provides the calculated peak CE for wavelengths ranging from 1530 to 1570 nm. The corresponding peak wavelengths for the two contour maps are illustrated in Figs. 3(c) and 3(d), suggesting the proposed PS-DBGC could be used for various wavelength schemes in the targeted wave bands. As marked by the pentagram in Fig. 3, a parameter set (Λ, DC) = (644 nm, 0.16) is chosen as it exhibits high CEs for both wavelength bands. It can also be seen from Fig. 3 that a larger period or duty cycle can redshift the peak wavelengths.

In addition to Λ and DC, the peak CEs of the PS-DBGC vary with the number of periodic squares, which is due to the overlap between the fundamental mode of the SMF and the diffracted field. As shown in Fig. 4(a), the peak CEs for both the O- and C-band will first increase and then decrease when the period number is growing. Hence, the number of periodic squares is

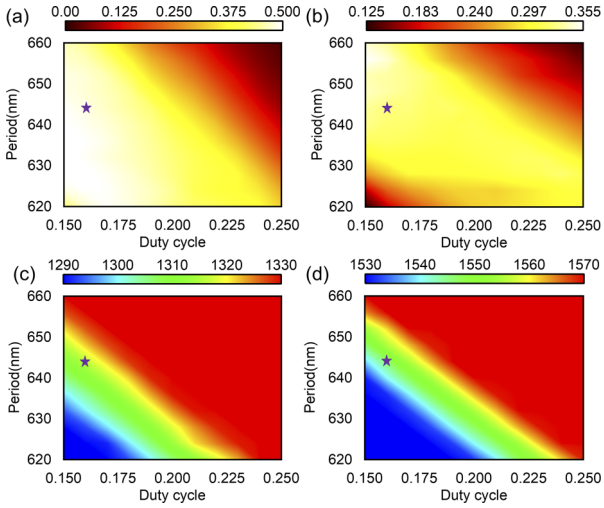

Fig. 3. Parametric sweep for PS-DBGC, simulated for two wavelength bands separately using the same fiber angle and position. (a), (b) Contour maps of peak CEs as a function of Λ and DC for the O- and C-band. (c), (d) Corresponding peak wavelengths for panels (a), (b).

set to 15 for the maximum average CE of both wave bands. Figures 4(b) and 4(c) show the calculated CE spectra of different polarizations as a function of wavelength for the O- and C-band, respectively. For X-/Y-/S-/P-polarization at 1310 nm, the calculated CEs are −3.1 dB, −3.1 dB, −3.1 dB, and −2.8 dB, respectively. In contrast, the calculated CEs are −4.9 dB, −4.8 dB, −4.6 dB, and −4.9 dB for X-/Y-/S-/P-polarization at 1550 nm, respectively. It is worth noting that the CE spectra of X-/Y-/S-/P-polarization have little difference and a very small polarization-dependent loss (PDL) ~ 0.3 dB can be obtained for all the polarizations. For all cases, the simulated 3-dB bandwidths are ~56 nm for the O-band and ~82 nm for the C-band, respectively. Electric-field profiles at peak wavelengths under different input polarizations are shown in Figs. 4(d) and 4(e). Coupled power is distributed in port-1 and port-2 for O-band X-polarization and Y-polarization (port-3 and port-4 for C-band X-polarization and Y-polarization), respectively. In addition, S-polarization and P-polarization are equally distributed into port-1 and port-2 for the O-band (port-3 and port-4 for the C-band), enabling uniform polarization splitting at both wave bands.

The device layout is patterned by a 100-keV electron beam lithography tool (Vistec EBPG 5000plus ES). As the etch depth is uniform for the entire device, a one-step etching process is employed and subsequently a 1-μm-thick silicon dioxide film is deposited using plasma-enhanced chemical vapor deposition (PECVD) to form the top silica cladding. As shown in Fig. 5(a), the performance of the PS-DBGC is experimentally verified by measuring the loss of two PS-DBGCs back-to-back connected at their operating ports. Taking the O-band light with X-polarization as an example, the transmitted spectra were measured through back-to-back connected port-1, while the transmitted spectra of back-to-back connected port-2 were also recorded as cross talk. Using the same approach, the transmission spectra of the O-band light with Y-polarization, and the C-band light with X-polarization and Y-polarization can be measured. Two continuous wave tunable lasers (Santec TSL-550 for the O-band and Santec TSL-710 for the C-band)

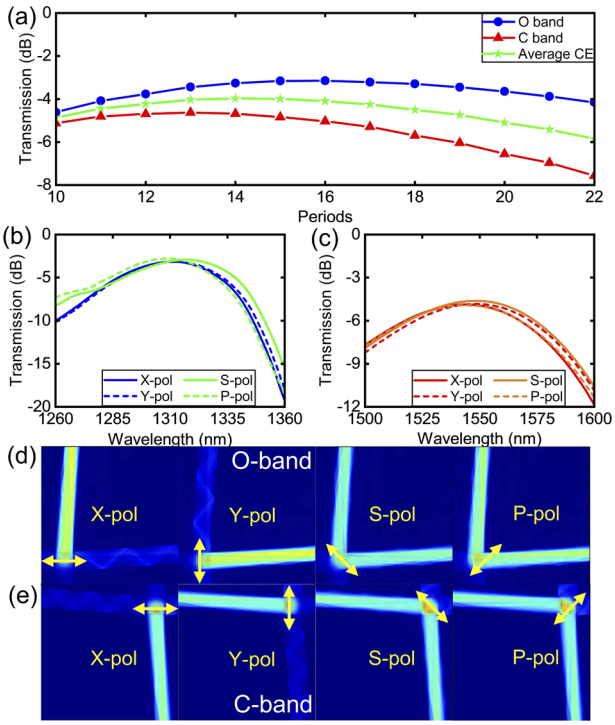

Fig. 4. (a) Calculated peak CEs and average CE for the O- and C-band with varied periods. (b), (c) Simulated CE spectrum for two wavelength bands with different polarizations. Simulated light propagation at wavelengths of (d) 1310 nm and (e) 1550 nm for X-/Y-/S-/P-polarizations.

are employed to sweep the 1260–1360-nm and 1480–1640-nm wavelength range, respectively. The light is coupled into and out of the chip via the PS-DBGC, and the CEs of the device are characterized as CE= $(P_{out} - P_{in})/2$, where P_{out} and P_{in} are the out-coupled and input power, respectively. A polarization controller (PC) is used to adjust an appropriate polarization state. The tilted angle and position of the fiber are kept the same for the two wavelength bands for all the measurements. The optical microscopy and enlarged SEM images of the fabricated PS-DBGC are shown in Fig. 5(b). By adjusting the PC, peak CEs of −4.7 dB and −5.2 dB are obtained at 1279 nm and 1280 nm, while CEs of −8.4 dB and −8.8 dB are obtained at 1522 nm

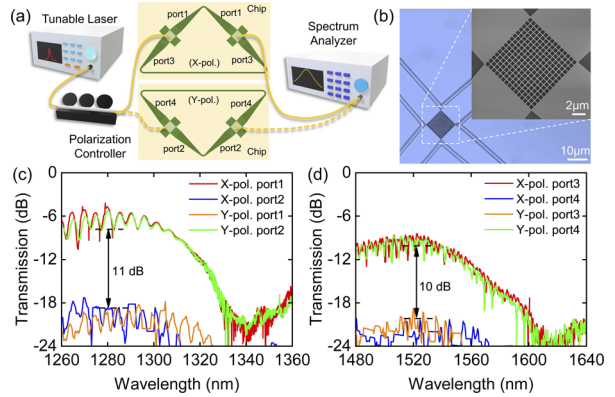

Fig. 5. (a) Experimental setup for verifying the performance of PS-DBGC. (b) Optical microscopy and SEM images of the fabricated PS-DBGC. Measured CEs of X-polarization and Y-polarization for the (c) O-band and (d) C-band.

Table 1. Simulated and Experimental CEs and Polarization Diversity (PD) of Demonstrated DBGCs near λ_1 and λ_2

Wavelength	Simulated	Experimental	PD
λ_1/λ_2/nm	CE_1/CE_2/dB	CE_1/CE_2/dB	Refs.
1280/1600	-4.3/-2.7	-4.3/-4.6	No [11]
1485/1530	NA	-6.5/-6	No [12]
1290/1521	-3.7/-3.4	-3.8/-5.4	Yes[a] [13]
1296/1576	-7.7/-6.7	-8.2/-7.1	Yes [21]
1280/1522	-2.8/-4.6	-4.7/-8.4	Yes [★]

★ This work.
[a]Polarization diversity is only for the C-band.

and 1516 nm for X- and Y-polarization, respectively. The CE spectra for the PS-DBGC are recorded as shown in Figs. 5(c) and 5(d). The corresponding 3-dB bandwidths are ∼43 nm and ∼52 nm for the O- and C-band, respectively. The cross talk at the center wavelengths is ∼11 and 10 dB for the O- and C-band, respectively, suggesting that the light with X- or Y- polarization is coupled to the corresponding waveguide. The measured spectra exhibit certain oscillation ripples for both wave bands, which we attribute to the grating backreflection induced Fabry–Perot interference. The connecting waveguide of the C-band is longer than that of the O-band, thus resulting in a smaller period. An additional Bragger grating structure can be introduced to further alleviate the backreflection [24]. There is a slight deviation of ∼30 nm between the measured and simulated center wavelengths, which can be attributed to the fabrication variations of etch depth. We anticipate that higher CEs can be achieved by optimizing etching depth and fabrication processes.

Table 1 shows a comparison of the performance of state-of-the-art DBGCs. A three-port GC is used in Ref. [13], thus providing polarization diversity only for one wave band. It is worth noticing that in Ref. [21], polarization-diversity operation is achieved using both TE and TM modes. Compared with these DBGCs in previous works, our PS-DBGC exhibits comparable CEs at both wavelength windows as the polarization-diversity DBGCs. Similar to conventional GCs, the CEs of this PS-DBCG can be improved by optimizing the fabrication processes or enhancing the directivity using reflectors on the substrate [25]. In addition, introducing an SWG structure could control the effective refractive index to achieve broadband operation bandwidth [14]. However, these approaches will increase the design and fabrication complexity. Furthermore, our work represents the first demonstration of a bi-wavelength PSGC using only the TE mode in the integrated waveguide, which will ease the on-chip polarization handling.

In conclusion, we propose and design a PS-DBGC that operates at the O- and C-band. The device relies on a square grating section with periodically arranged square holes with four output ports to achieve dual-wavelength-band polarization-diversity operation. For different polarizations, simulation results show maximum CEs of −2.8 dB at 1310 nm and −4.6 dB at 1550 nm. For the fabricated device, the measured central wavelengths are near 1280 nm and 1522 nm, and the peak CEs are −4.7 dB and −8.4 dB, respectively. With further optimization and standard packaging technologies, we expect that our proposed PS-DBGC will be useful for providing a cost-efficient optical fiber to chip coupling components for future integrated WDM-PON systems.

Funding. National Natural Science Foundation of China (51874301, 61904204, 62175080); Key Research and Development Program of Hubei Province (2021BAA005).

Acknowledgments. The authors thank ShanghaiTech University Quantum Device Lab and the Center of Micro-Fabrication and Characterization (CMFC) of Wuhan National Laboratory for Optoelectronics for device fabrication and characterization.

Disclosures. The authors declare no conflicts of interest.

Data availability. Data underlying the results presented in this paper are not publicly available at this time but may be obtained from the authors upon reasonable request.

REFERENCES

1. H. Ishio, J. Minowa, and K. Nosu, J. Lightwave Technol. **2**, 448 (1984).
2. J. S. Wey, J. Lightwave Technol. **38**, 31 (2020).
3. X. Guan, W. Shi, J. Liu, P. Tan, J. Slevinsky, and L. A. Rusch, IEEE Commun. Mag. **59**, 126 (2021).
4. A. Banerjee, Y. Park, F. Clarke, H. Song, S. Yang, G. Kramer, K. Kim, and B. Mukherjee, J. Opt. Netw. **4**, 737 (2005).
5. D. Taillaert, W. Bogaerts, P. Bienstman, T. Krauss, P. Van Daele, I. Moerman, S. Verstuyft, K. De Mesel, and R. Baets, IEEE J. Quantum Electron. **38**, 949 (2002).
6. D.-X. Xu, J. H. Schmid, G. T. Reed, G. Z. Mashanovich, D. J. Thomson, M. Nedeljkovic, X. Chen, D. Van Thourhout, S. Keyvaninia, and S. K. Selvaraja, IEEE J. Sel. Top. Quantum Electron. **20**, 189 (2014).
7. X. Chen, K. Xu, Z. Cheng, C. K. Y. Fung, and H. K. Tsang, Opt. Lett. **37**, 3483 (2012).
8. A. Sánchez-Postigo, J. G. Wangüemert-Pérez, J. M. Luque-González, Í. Molina-Fernández, P. Cheben, C. A. Alonso-Ramos, R. Halir, J. H. Schmid, and A. Ortega-Mo nux, Opt. Lett. **41**, 3013 (2016).
9. G. Roelkens, D. V. Thourhout, and R. Baets, Opt. Express **15**, 10091 (2007).
10. G. Roelkens, D. Vermeulen, S. Selvaraja, R. Halir, W. Bogaerts, and D. Van Thourhout, IEEE J. Sel. Top. Quantum Electron. **17**, 571 (2011).
11. D. González-Andrade, D. Pérez-Galacho, M. Montesinos-Ballester, X. L. Roux, E. Cassan, D. Marris-Morini, P. Cheben, N. Vulliet, S. Monfray, F. Boeuf, L. Vivien, A. V. Velasco, and C. Alonso-Ramos, Opt. Lett. **46**, 617 (2021).
12. L. Xu, X. Chen, C. Li, and H. K. Tsang, Opt. Commun. **284**, 2242 (2011).
13. L. Cheng, S. Mao, Z. Li, X. Tu, and H. Y. Fu, Opt. Lett. **46**, 3308 (2021).
14. W. Zhou, Z. Cheng, X. Sun, and H. K. Tsang, Opt. Lett. **43**, 2985 (2018).
15. W. Zhou and H. K. Tsang, Opt. Lett. **44**, 3621 (2019).
16. W. S. Zaoui, A. Kunze, W. Vogel, and M. Berroth, IEEE Photonics Technol. Lett. **25**, 1395 (2013).
17. J. Zou, Y. Yu, and X. Zhang, Opt. Express **23**, 32490 (2015).
18. T. Watanabe, Y. Fedoryshyn, and J. Leuthold, IEEE Photonics J. **11**, 1 (2019).
19. Y. Xue, H. Chen, Y. Bao, J. Dong, and X. Zhang, Opt. Express **27**, 22268 (2019).
20. B. Chen, X. Zhang, J. Hu, Y. Zhu, X. Cai, P. Chen, and L. Liu, Opt. Express **28**, 4001 (2020).
21. M. Streshinsky, R. Shi, A. Novack, R. T. P. Cher, A. E.-J. Lim, P. G.-Q. Lo, T. Baehr-Jones, and M. Hochberg, Opt. Express **21**, 31019 (2013).
22. T. Hao, A. Sánchez-Postigo, P. Cheben, A. Ortega-Mo nux, and W. N. Ye, IEEE Photonics Technol. Lett. **32**, 1163 (2020).
23. W. Bogaerts, D. Taillaert, P. Dumon, D. V. Thourhout, R. Baets, and E. Pluk, Opt. Express **15**, 1567 (2007).
24. D. Hu, Y. Zhang, Y.-Y. Zhao, and X.-M. Duan, Opt. Express **30**, 2131 (2022).
25. F. Van Laere, G. Roelkens, M. Ayre, J. Schrauwen, D. Taillaert, D. Van Thourhout, T. F. Krauss, and R. Baets, J. Lightwave Technol. **25**, 151 (2007).